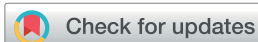


## PAPER



Cite this: *J. Mater. Chem. A*, 2023, **11**, 11463

## Secondary interaction-manipulated metal–organic crystalline nanotube array for gas sensing†

Jieying Hu,<sup>‡a</sup> Jian-Ze Xiao,<sup>‡b</sup> Wei-Ming Liao,<sup>‡c</sup> Shoujie Liu,<sup>‡c</sup> Jianming Li,<sup>a</sup> Yonghe He,<sup>a</sup> Lin Yu,<sup>‡a</sup> Qiaohong Li,<sup>‡b</sup> Gang Xu<sup>‡bde</sup> and Jun He<sup>‡\*a</sup>

Although having attracted growing interest, the design and preparation of metal–organic crystalline nanotube arrays (MO-CNAs) remains a challenge. Herein, a Pb···S metal–nonmetal secondary interaction strategy was proposed to prepare a Pb(II)-based MO-CNA (Pb-HTT), endowing Pb-HTT with high thermal/chemical stability, a porous structure, and open metal sites. With unique unsaturated metal centers for guest accommodation, Pb-HTT exhibited the best sensing performance with both response time <0.1 min and theoretical limit of detection <0.1 ppb in comparison to all reported room-temperature NO<sub>2</sub> chemiresistive sensing materials. It also showed highly selective sensing toward NO<sub>2</sub> among 10 interfering gases. The experimental XANES data and theoretical calculation verified the exact active sites of Pb centers on Pb-HTT and revealed the sensing mechanism. Notably, this study not only provides a useful metal–nonmetal secondary interaction strategy for the construction of MO-CNAs, but also accelerates the application of semiconducting CNAs in structure-directed functional electronic devices.

Received 10th March 2023  
Accepted 28th April 2023

DOI: 10.1039/d3ta01475d

rsc.li/materials-a

## Introduction

The great success of carbon nanotubes, especially in electronics, has sparked off the syntheses of many novel nanotube-structured materials for exploring broader and better applications.<sup>1</sup> Enormous effort has been put into developing crystalline nanotube arrays (CNAs), which provide phase-pure nanotubes and atomic-level precision in structures.<sup>2–5</sup> At present, some inorganic,<sup>6,7</sup> organic,<sup>8,9</sup> and metal–organic CNAs<sup>10–12</sup> have been prepared, but unlike carbon nanotubes, few CNAs show electronically conducting properties, let alone the potential for application in electronic devices.

Metal–organic crystalline nanotube arrays (MO-CNAs) are constructed by the coordination bonds among organic ligands and metal ions.<sup>13,14</sup> MO-CNAs also refer to the discrete ones without any coordination or covalent bonds to neighboring tubes. Compared with other CNAs, MO-CNAs have more specially designed structures and intriguing physical/chemical properties.<sup>2,15</sup> However, due to the complicated coordination-bond formation during the self-assembly process, the designable synthesis of MO-CNAs *via* bottom-up or *in situ* approaches still faces a great challenge. The main difficulty lies in the fact that the construction of a one-dimensional (1D) channel and blocking the coordination among neighboring nanotubes should be achieved simultaneously to generate MO-CNAs. Infinite 1D channels can be obtained from the well-explored coordination assembly of flexible helical,<sup>16–18</sup> macrocyclic,<sup>19–21</sup> and multitopic<sup>12,22–24</sup> linkers with related metal ions.<sup>25</sup> However, most metal ions adopt a multi-coordination mode and hence 2D and 3D coordination polymers are preferred over 1D MO-CNAs. To tackle this issue, ancillary terminal ligands (H<sub>2</sub>O,<sup>7,26</sup> DMF,<sup>27</sup> ethylenediamine (EDA),<sup>28</sup> *N*-methylformamide,<sup>29</sup> *etc.*) are used to occupy the partial coordination sites of metal ions to terminate further coordination. However, the introduction of these secondary ligands often leads to a more complicated and uncontrollable coordination assembly, hindering the formation of the target structure. Moreover, these secondary ligands saturate the coordination number of the metal ions, impeding MO-CNAs in applications utilizing the open metal sites, such as in catalysis and sensing. A structure-design strategy to construct

<sup>a</sup>School of Chemical Engineering and Light Industry, Guangdong University of Technology, Guangzhou, 510006, P. R. China. E-mail: junhe@gdut.edu.cn; wmliao@gdut.edu.cn

<sup>b</sup>State Key Laboratory of Structural Chemistry, Fujian Institute of Research on the Structure of Matter, Chinese Academy of Sciences, Fuzhou, 350002, P. R. China. E-mail: gxu@fjirsm.ac.cn

<sup>c</sup>Chemistry and Chemical Engineering of Guangdong Laboratory, Shantou, 515063, P. R. China

<sup>d</sup>University of Chinese Academy of Sciences, Beijing, 100049, P. R. China

<sup>e</sup>Fujian Science & Technology Innovation Laboratory for Optoelectronic Information of China, Fuzhou, 350108, P. R. China

† Electronic supplementary information (ESI) available: General experimental details, SEM, single crystal structure, NMR spectra, XPS, FT-IR, TGA, BET, CBM, VBM, NO<sub>2</sub> sensing curves, DFT calculation and crystal data (CIF). CCDC 2129174. For ESI and crystallographic data in CIF or other electronic format see DOI: <https://doi.org/10.1039/d3ta01475d>

‡ These authors contributed equally to this work.

MO-CNAs with accessible open metal sites is thus extremely desired.

Secondary interactions refer to those with a strength weaker than coordination bonds or covalent bonds.<sup>30,31</sup> Some common secondary interactions based on metal–metal or nonmetal–nonmetal units, such as hydrogen bonds,<sup>32,33</sup>  $\pi$ – $\pi$  stacking interactions,<sup>34,35</sup> and silver–silver interactions,<sup>36</sup> have been employed for the construction of supramolecular structures. Nevertheless, metal–nonmetal-based secondary interactions with a stronger strength than hydrogen bonds and  $\pi$ – $\pi$  stacking, are rarely taken into account for structure construction, especially for MO-CNAs design. This kind of secondary interaction is, however, beneficial to “saturate” the coordination number of metal sites, while the longer metal–nonmetal distances can provide extra space for guest species to interact with the unsaturated metal sites.

In this work, we propose the first use of a metal–nonmetal-based secondary interaction strategy for constructing MO-CNAs to meet the above-mentioned challenges. The heavy p-block Pb(II) ion was selected as the metal species due to its variable coordination-bond distances, and non-covalent secondary interactions with nonmetal atoms. The  $\pi$ -conjugated linker HTT<sup>6-</sup> (triphenylene-2,3,6,7,10,11-hexakis(thiolate)) was selected since (1) its trigonal geometry makes it an ideal  $\mu_3$ -bridging ligand to build MO-CNAs, and (2) the extended  $\pi$ -conjugated structure is well-known for building semiconducting coordination polymers. Taking advantage of Pb $\cdots$ S secondary interactions, the coordination between Pb and HTT<sup>6-</sup> gave rise to a new MO-CNA, namely **Pb-HTT** (Fig. 1). With accessible metal sites from the unsaturated coordination of Pb centers, **Pb-HTT** was applied for chemiresistive NO<sub>2</sub> sensing. Gratifyingly, this represents the first room-temperature NO<sub>2</sub>

sensing material with both a response time <0.1 min and theoretical LOD <0.1 ppb. Notably, it is also the first secondary interaction-based CNA demonstrating an application in structure-directed functional electronic devices.

## Experimental section

### Synthesis and activation of Pb-HTT

A 25 mL Schlenk tube was loaded with HVaTT (36.4 mg, 0.04 mmol) and then evacuated and back-filled with nitrogen gas three times. Dry DMF (4 mL) and MeOH (4 mL) were bubbled through with nitrogen for 5 min and injected in to the flask. Then the mixture was sonicated until HVaTT was completely dissolved. A solution of Pb(OAc)<sub>2</sub>·3H<sub>2</sub>O (45.6 mg, 0.12 mmol) in ethylenediamine (8.0 mL) was bubbled through with nitrogen for 5 min and then added into the Schlenk tube. The obtained mixture was heated at 90 °C in an oven for 24 h followed by allowing it to cool to room temperature naturally. Yellow needle-like crystals were thus collected, which were washed with DMF (3 × 5 mL), methanol (3 × 5 mL), and acetone (3 × 5 mL), and evacuated at room temperature to obtain the as-synthesized **Pb-HTT**. For activating the sample, the as-synthesized **Pb-HTT** was soaked in acetone (replaced by fresh acetone every 4 h) at 60 °C for 24 h, then separated and dried at 70 °C under vacuum. Elemental analysis found C (25.69%), H (2.81%), and N (6.84%), thus fitting the formula of [Pb<sub>5</sub>(HTT)<sub>2</sub>(C<sub>2</sub>N<sub>2</sub>H<sub>9</sub>)<sub>2</sub>]·3.2C<sub>2</sub>N<sub>2</sub>H<sub>8</sub>·0.39C<sub>3</sub>H<sub>7</sub>NO·0.95CH<sub>3</sub>OH·2H<sub>2</sub>O; calculated: C (25.62%), H (2.93%), and N (6.64%).

### Device fabrication

Gas sensor devices were fabricated by a typical drop-casting method. Initially, a proper amount of the as-prepared **Pb-HTT**

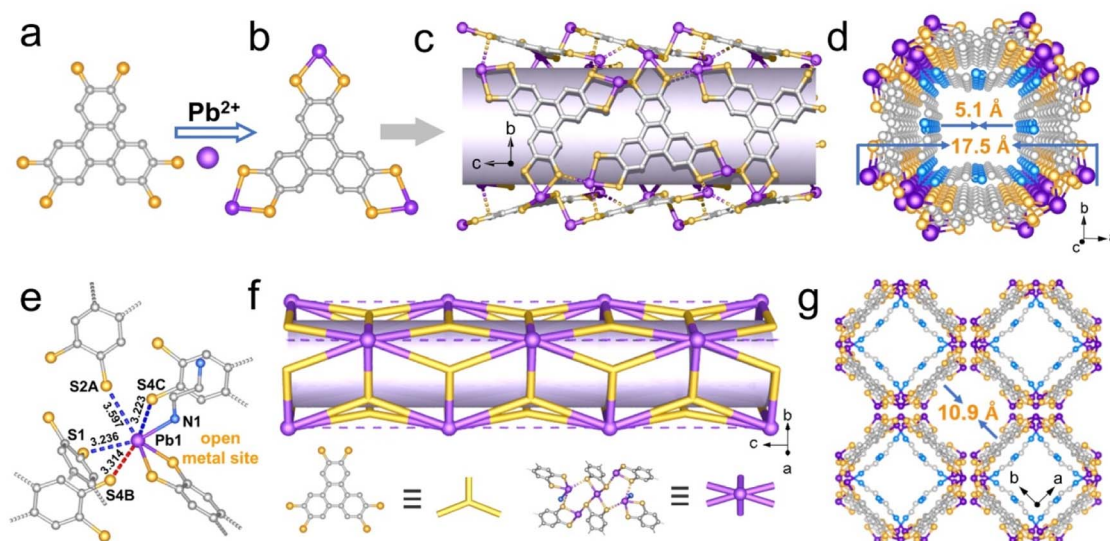


Fig. 1 Single-crystal structure of **Pb-HTT**. (a) Three-connected linker HTT<sup>6-</sup>. (b) Y-type Pb<sub>3</sub>(HTT) coordination geometry. (c) Flank view of a single nanotube. Cylinder represents the inside channel after omitting EDA species. (d) Single nanotube viewed along the *c*-axis. (e) Coordination environment and secondary interactions of Pb1 centers. Blue and red dots represent intra-tube and inter-tube secondary interactions, respectively. (f) Simplified topology network. (g) Packing diagram of the nanotube array of **Pb-HTT** along *c*-axis. Atom color: Pb purple, C gray, S yellow, N blue.

crystal was mixed with absolute isopropanol and ground in an agate mortar to form a slurry. Then the slurry was coated on pre-cleaned Ag–Pd interdigitated electrodes with a gap width of 200  $\mu\text{m}$ , in which  $\text{Al}_2\text{O}_3$  ceramic was used as the sensor substrate (7 mm  $\times$  13.5 mm). The coated slurry was naturally dried to form a uniform sensing layer at room temperature, while two gold wires were attached to each side of the interdigitated electrodes *via* a silver conductive paste. Then, the sensor devices were aged in a vacuum oven at 60  $^\circ\text{C}$  for 1 h before the sensing tests.

### Gas sensing tests

The gas sensing tests were carried out on a homemade gas sensing test system. A constant bias voltage of 5 V was applied on the device while the current was measured by a source meter (Keithley 2602B) in real time. We started the measurement by purging the chamber with dry synthetic air (21% oxygen/79% nitrogen) for 2 h. The gas flow of air and analytes diluted in air was controlled at 600 sccm by mass flow controllers (MFCs). The response value is defined as  $I_g/I_0 - 1$ , where  $I_g$  is the device current upon exposure to the gas analytes and  $I_0$  is the baseline device current. The response or recovery time was defined as the time taken to reach 90% of the total current value change.

## Results and discussion

### MO-CNA synthesis and structure characterization

The linker precursor 2,3,6,7,10,11-hexakis(pentanoylthio)triphenylene (HVaTT)<sup>37</sup> (Fig S1 and S2<sup>†</sup>) was elaborately selected to mix with  $\text{Pb}(\text{OAc})_2$  and then heated solvothermally in EDA/MeOH/DMF. HVaTT was hydrolyzed *in situ* to  $\text{HTT}^{6-}$  species (Fig. 1a) and then coordinated to  $\text{Pb}^{\text{II}}$  ions,<sup>38</sup> affording yellow needle-like crystals of **Pb-HTT** (Fig. 2a, b and S3<sup>†</sup>). The structure of **Pb-HTT** was determined by single-crystal X-ray diffraction (SCXRD). It crystallized in the tetragonal system with the space group  $P4/ncc$  (Table S1<sup>†</sup>). A solvent mask was calculated and 1478 electrons were found in a volume of 5911  $\text{\AA}^3$  per unit cell, indicating the formula of  $[\text{Pb}_5(\text{HTT})_2(\text{C}_2\text{N}_2\text{H}_9)_2] \cdot 3.5\text{C}_2\text{N}_2\text{H}_8 \cdot 0.4\text{C}_3\text{H}_7\text{NO} \cdot \text{CH}_3\text{OH} \cdot 2\text{H}_2\text{O}$  for **Pb-HTT**. The asymmetric unit of **Pb-HTT** consisted of three crystallographically independent  $\text{Pb}^{\text{II}}$  ions with occupancies of 1, 1, and 1/2, one  $\text{HTT}^{6-}$  linker, and one coordinated EDA species in which one amino-group was protonated for charge balance (Fig. S4<sup>†</sup>).  $\text{HTT}^{6-}$  expectedly served as a 3-connected linker bridging three  $\text{Pb}^{\text{II}}$  ions to form Y-type  $\text{Pb}_3(\text{HTT})$  coordination geometry (Fig. 1b). This rigid  $\text{Pb}_3(\text{HTT})$  plane was quite appropriate for acting as the nanotube wall through a tiling arrangement.

According to the search results for the CCDC database and related papers (Fig. S5 and Table S2<sup>†</sup>),  $\text{Pb} \cdots \text{S}$  secondary interactions could be tentatively attributed to the interaction with a  $\text{Pb} \cdots \text{S}$  distance longer than 3.20  $\text{\AA}$  (ref. 39) and shorter than the sum of Pb and S van der Waals radii of 3.80  $\text{\AA}$ ,<sup>31,40</sup> though the lower limit fluctuated slightly. It was this secondary interaction that induced the formation of a single-wall nanotube containing a 1D channel of about  $5.1 \times 5.1 \text{\AA}^2$  (Fig. 1c and d). In the coordination environments of Pb centers, Pb1 is tricoordinated

to two S atoms and one N atom, while Pb2 and Pb3 are respectively four-coordinated and tricoordinated to S atoms (Fig. 1e, S6 and S7<sup>†</sup>). All the  $\text{Pb} \cdots \text{S}$  coordination bonds have lengths less than 2.968  $\text{\AA}$ . Importantly, all these Pb ions have an unsaturated coordination with considerable open sites. These open metal sites are further stabilized by the abundant  $\text{Pb} \cdots \text{S}$  secondary interactions with the distance varying from 3.223 to 3.597  $\text{\AA}$ . In detail, Pb1 interacts with S4B, S1, S4C, and S2A with the  $\text{Pb} \cdots \text{S}$  distances of 3.314, 3.236, 3.223, and 3.597  $\text{\AA}$ , while Pb2 interacts with S5B and S5D with the same  $\text{Pb} \cdots \text{S}$  distance of 3.477  $\text{\AA}$ , and Pb3 interacts with S5D with the  $\text{Pb} \cdots \text{S}$  distance of 3.317  $\text{\AA}$ . From a topological perspective, a metal center can be defined as a 6-connected node which is in contact with six nearest linkers and the nanotube can be simplified into a 1D network (Fig. 1f).

$\text{Pb} \cdots \text{S}$  secondary interactions play important roles from the intra-tube and inter-tube points of view (Fig. S8<sup>†</sup>): (1) endowing the appropriate spatial orientation for  $\text{Pb}_3(\text{HTT})$  tiling by their moderate strength and flexible interaction distance. All these three kinds of Pb ions are located in the connecting chains while  $\text{HTT}^{6-}$  linkers stand in the tiling planes, which ensures a tetragonal geometry of the nanotube; (2) saturating some Pb coordination sites and preventing the formation of a multidimensional coordination structure. The secondary interactions coupling with coordination bonds make the interaction numbers of Pb1, Pb2, and Pb3 be up to 7, 6, and 4, respectively, probably leading to a more stable 1D coordination framework. Meanwhile, the accessible  $\text{Pb}^{\text{II}}$  metal sites serve as excellent platforms for studying the role of the metal center on guest molecule binding; (3) assisting the aggregation of 1D nanotubes into a 3D MO-CNA structure and endowing this with a higher robustness than in traditional MO-CNAs bearing weak secondary interactions (*e.g.*, hydrogen bonds) among neighboring nanotubes.<sup>41,42</sup> Notably, a large inter-tube channel (10.9  $\times$  10.9  $\text{\AA}^2$ ) is formed by every four nanotubes (Fig. 1g). Calculated by the PLATON program,<sup>43</sup> **Pb-HTT** was found to possess a large porosity of 40.8%. Both the open metal sites and inter-tube space provide sufficient conditions for interaction with guest molecules.

### General characterization

The elemental analysis (EA) data could be fitted by the formula of  $[\text{Pb}_5(\text{HTT})_2(\text{C}_2\text{N}_2\text{H}_9)_2] \cdot 3.2\text{C}_2\text{N}_2\text{H}_8 \cdot 0.39\text{C}_3\text{H}_7\text{NO} \cdot 0.95\text{CH}_3\text{OH} \cdot 2\text{H}_2\text{O}$  for **Pb-HTT**, which is quite close to that obtained from crystal data. EDA amount was also verified by  $^1\text{H}$  NMR spectroscopy (Fig. S9 and S10<sup>†</sup>). Elemental mapping images indicate that Pb, S and N elements are distributed uniformly (Fig. S11<sup>†</sup>). X-ray photoelectron spectroscopy (XPS) analysis demonstrates Pb 4f detailed spectra in Fig. S12b (see ESI).<sup>†</sup> The peaks at 138.41 and 143.27 eV are assigned to Pb 4f<sub>7/2</sub> and 4f<sub>5/2</sub>, respectively, which correspond to the characteristic signals of  $\text{Pb}^{2+}$ .<sup>38,44</sup> HVaTT and **Pb-HTT** differ in FT-IR spectra, indicating the hydrolysis of linkers and successful coordination between  $\text{Pb}^{2+}$  and  $\text{HTT}^{6-}$  (Fig. S13<sup>†</sup>). Consistent PXRD patterns and further Rietveld refinement both suggested good phase purity of as-synthesized **Pb-HTT** (Fig. S14 and S15<sup>†</sup>). High-resolution

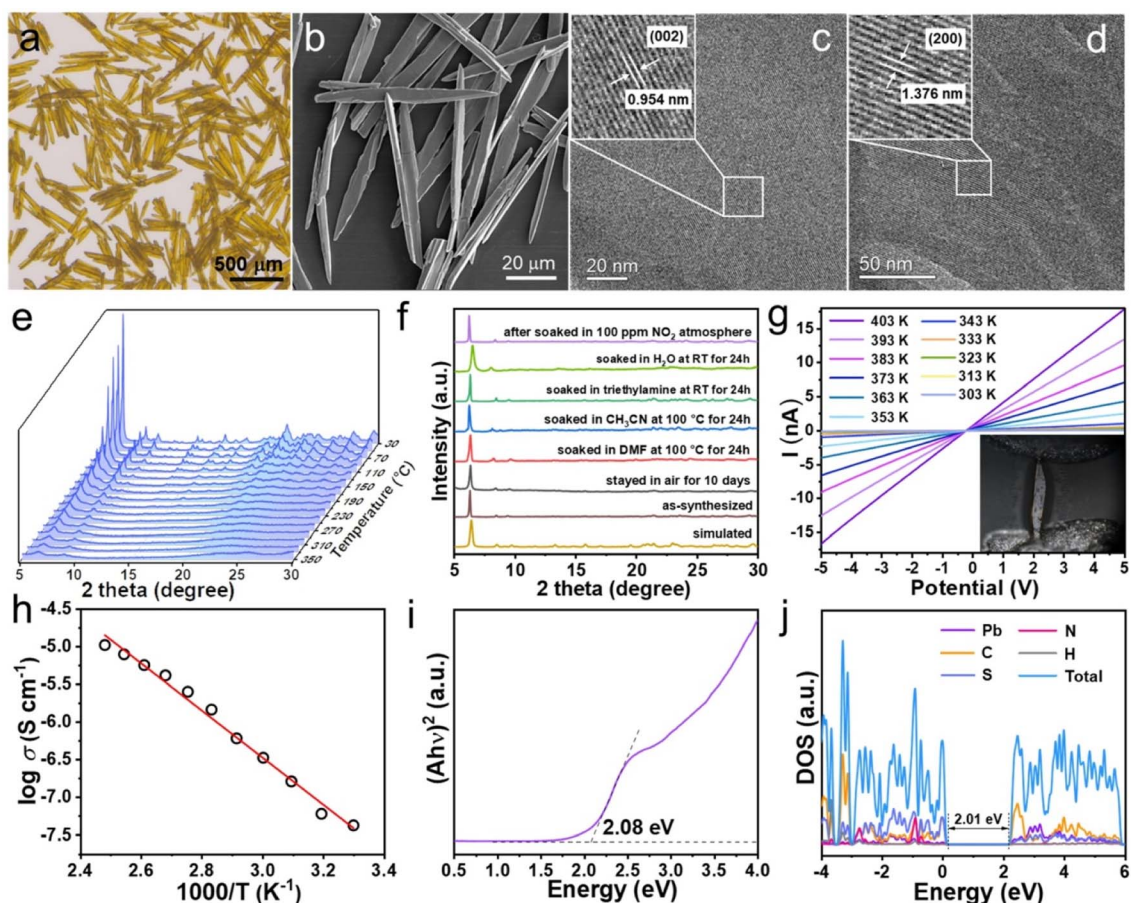


Fig. 2 General characterizations and studies of Pb-HTT. (a) Photograph, (b) SEM image, and (c and d) HRTEM images of Pb-HTT. (e) *In situ* variable-temperature PXRD patterns of Pb-HTT varying from 30 °C to 350 °C. (f) PXRD patterns of Pb-HTT after treatment under different conditions. (g) *I*–*V* voltammetric curves at different temperatures (inset: photograph of a single crystal equipped for the conductivity measurement). (h) Arrhenius plots with linear fitting of  $\log \sigma$  to  $1000/T$ . (i) Tauc plot. (j) Projected density of states (PDOS).

transmission electron microscope (HRTEM) images show the lattice fringes of (002) and (200) with a spacing of 0.954 and 1.376 nm, respectively (Fig. 2c and d).

Thermogravimetric (TG) curves indicate Pb-HTT is thermally stable up to around 200 °C both in air and  $N_2$  atmosphere (Fig. S16 and S17<sup>†</sup>), which is supported by the temperature-dependent PXRD data (Fig. 2e). The framework remains intact after exposure to the air for 10 days or immersion in  $CH_3CN$ , DMF, triethylamine for 24 h (Fig. 2f).  $N_2$  adsorption and desorption experiments at 77 K reveal that Pb-HTT mainly belongs to type I isotherm (Fig. S18<sup>†</sup>), and the porous character endows Pb-HTT with potential for guest accommodation.

The electrical conduction (*I*–*V* curves) was measured using a two-probe method with single-crystal Pb-HTT at different temperatures (Fig. 2g). The electrical conductivities at ambient temperature (303 K) and 403 K were approximately  $4.22 \times 10^{-8}$  and  $1.04 \times 10^{-5} \text{ S cm}^{-1}$ , respectively. The good linearity of  $\log \sigma$  to  $1000/T$  indicated that electron conduction followed the Arrhenius equation (Fig. 2h). The band gap of 2.08 eV estimated from the Tauc plot (Fig. 2i) was quite close to the value of 2.01 eV predicted by density functional theory (DFT) calculation (Fig. 2j and S19<sup>†</sup>).<sup>45,46</sup> The temperature-dependent electrical

conductivity and appropriate optical band gap indicated the semiconductive nature of Pb-HTT.

### Gas sensing tests

At present, most chemiresistive gas sensing materials can only achieve performance under high temperature, light irradiation conditions, or in composite systems. It is still a large challenge to construct single-phase gas sensors with high sensitivity, fast response/recovery, and exclusive selectivity. With unique secondary interaction-manipulated Pb centers and an accessible inner-surface from the ordered 1D channels, Pb-HTT could be expected to exhibit unprecedented room-temperature sensing performance.

Herein, nitrogen dioxide ( $NO_2$ ) was selected as an analyte, because it is an important air pollutant. Recently, it was also found that there are positive associations between the long-term exposure to ppb-level  $NO_2$  and the COVID-19 case-fatality rate and mortality rate.<sup>47,48</sup> The responses of Pb-HTT toward  $NO_2$  vs. other gases of  $CO_2$  and  $CH_4$ , were investigated using a homemade sensor device at room temperature (Scheme S1<sup>†</sup>). Pb-HTT showed the highest response to  $NO_2$ , even compared with the inference gases with a concentration 10 times higher

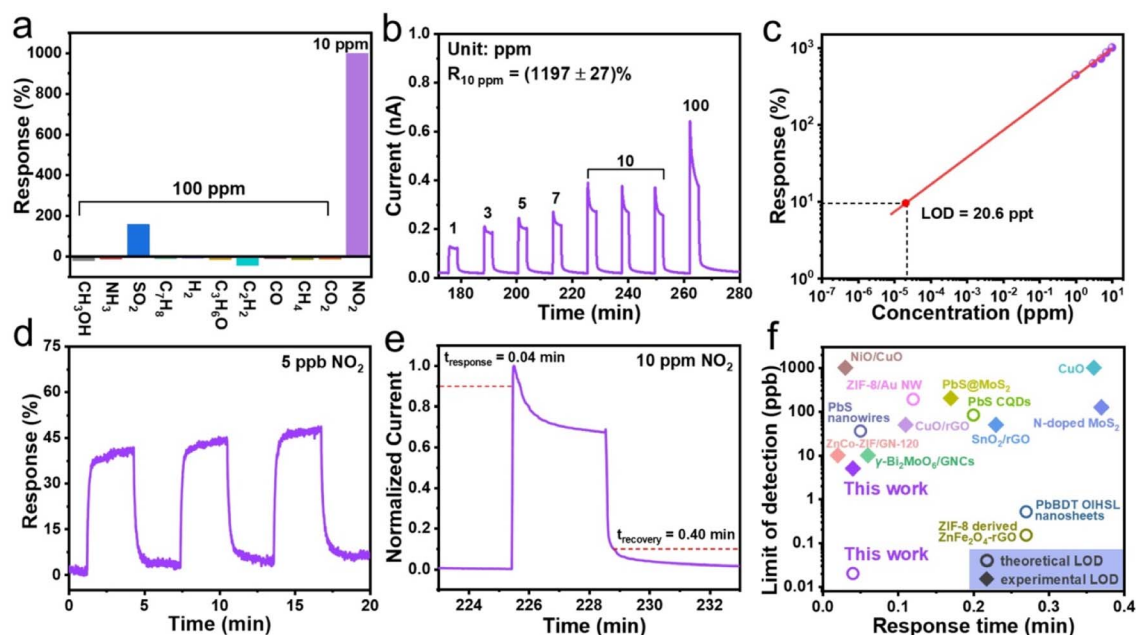


Fig. 3 Gas sensing without light assistance. (a) Chemiresistive selectivity from 10 other kinds of interference gases. (b) Response and recovery curves toward different concentrations of  $\text{NO}_2$ . (c) Log–log linear fitting of the response–concentration plot. (d) Response and recovery curves toward 5 ppb  $\text{NO}_2$ . (e) Response and recovery time toward 10 ppm  $\text{NO}_2$ . (f) Previously reported sensing materials with  $\text{NO}_2$  concentration less than 1 ppm and response time within 0.4 min.

than that of  $\text{NO}_2$ , indicating its high selectivity (Fig. 3a). It also exhibited a conspicuous response to a wide concentration range (1–100 ppm) of  $\text{NO}_2$  with a theoretical limit of detection (LOD) of 20.6 ppt with a response of 0.1 (Fig. 3b and c). Experimentally, **Pb-HTT** could detect  $\text{NO}_2$  with a concentration as low as 5 ppb (Fig. 3d and S20<sup>†</sup>). Moreover, **Pb-HTT** exhibited a very short response and recovery time. For example, the response and recovery time were only 0.04 and 0.4 min for 10 ppm  $\text{NO}_2$ , respectively, while they were 0.44 min and 0.77 min for 5 ppb  $\text{NO}_2$  (Fig. 3e and S21<sup>†</sup>). Notably, without light irradiation, **Pb-HTT** represents the first room-temperature  $\text{NO}_2$  sensing material with both response time <0.1 min and theoretical LOD <0.1 ppb (Fig. 3f and Table S3<sup>†</sup>).<sup>49–61</sup> Further, the framework remained intact after the sensing experiments according to the PXRD patterns (Fig. 2f).

### Sensing mechanism investigation

The semiconductive nature and strong  $\text{Pb}\cdots\text{NO}_2$  interaction may account for the sensing ability of **Pb-HTT** toward  $\text{NO}_2$ . The experimental XANES spectra of Pb K-edge were measured for PbS, **Pb-HTT**, and **Pb-HTT-NO<sub>2</sub>** (**Pb-HTT** treated with  $\text{NO}_2$ ) (Fig. 4a). The Pb edges were quite similar in these three samples, indicating the same valency of +2 for Pb. Specially, a slight blue shift (from 13 042.5 to 13 042.8 eV) of the edge energy was noticed on **Pb-HTT-NO<sub>2</sub>** when compared with **Pb-HTT**, suggesting a partial charge transfer from the Pb metal center to  $\text{NO}_2$  molecules.<sup>62,63</sup> A shortening of the average Pb–N or/and Pb–S distances was observable in *R*-space, where Fourier transform (FT)  $k^2$ -weighted  $\chi(k)$  showed its distance moving from 2.15 to 2.11 Å (Fig. 4b). The peak intensity increase at

around 2.11 Å reflected a slight framework rearrangement while maintaining an ordered higher shells signal.<sup>64</sup> Both the shortening of the above distances and the increase in peak intensities support the interaction between the Pb center and nitrogen atom of the  $\text{NO}_2$  gas.<sup>65</sup>

DFT calculations were also performed to verify the sensing process. The equilibrium lattice constants of the tetragonal **Pb-HTT** unit cell were first optimized when the *k*-point for Brillouin zone sampling was used. Different positions of gas molecules and the most energetically favorable configurations were then considered for the adsorption of various molecules ( $\text{NO}_2$ ,  $\text{SO}_2$ ,  $\text{CO}_2$ ,  $\text{CO}$ ). The adsorption energies ( $E_{\text{ads}}$ ) of different gas molecules on the surface of **Pb-HTT** were determined to be –0.63, –0.27, –0.17, and –0.04 eV for  $\text{NO}_2$ ,  $\text{SO}_2$ ,  $\text{CO}_2$ , and  $\text{CO}$ , respectively (Fig. 4c–f and S22–S24<sup>†</sup>). Meanwhile, after gas adsorption, the number of electrons transferred from **Pb-HTT** to the gas molecules was found to be 0.341, 0.074, 0.031, and 0.019 for  $\text{NO}_2$ ,  $\text{SO}_2$ ,  $\text{CO}_2$ , and  $\text{CO}$ , respectively. The lowest adsorption energy and largest electron transfer in the case of  $\text{NO}_2$  could have been responsible for the highly selective sensing of **Pb-HTT** to  $\text{NO}_2$  compared to the other gases. The DFT results also indicated that the interaction sites were located at the unsaturated Pb3 centers (Fig. 4c, d and 5). Both the experimental and theory studies revealed the preferable sensing ability of **Pb-HTT** to  $\text{NO}_2$  benefiting from the secondary interaction-manipulated unsaturated Pb centers and high affinity. Based on the above consideration, a sensing mechanism including the charge transfer state, saturation, and recovery state was proposed (Fig. 5).

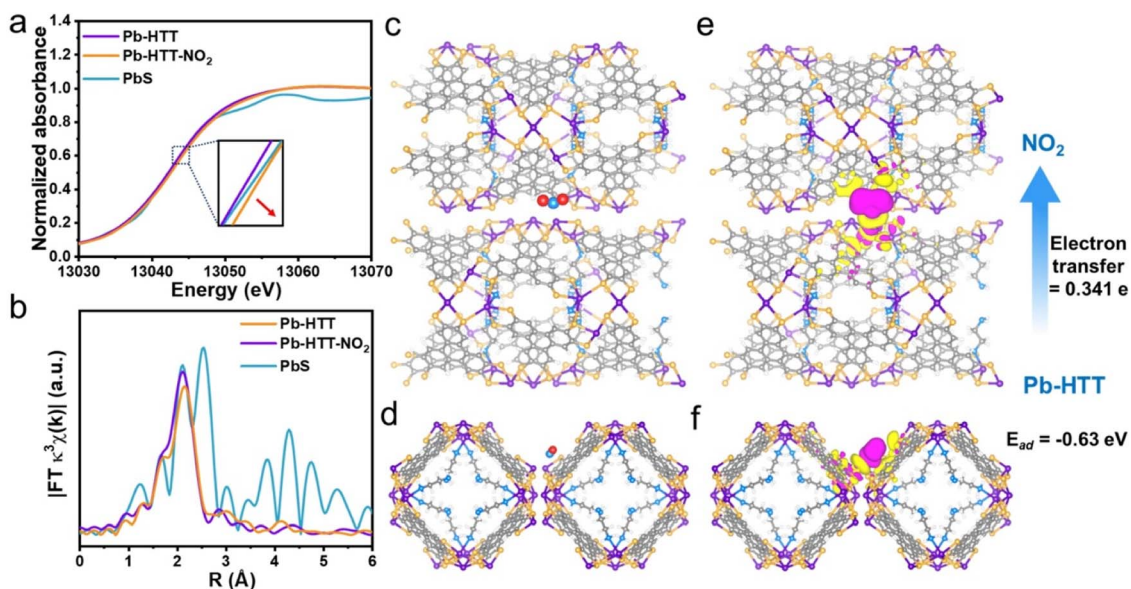


Fig. 4 XANES results, DFT calculation, and proposed sensing mechanism. (a) Pb K-edge XANES and (b) FT of EXAFS spectra of PbS, Pb-HTT, and Pb-HTT after exposure to NO<sub>2</sub>. Adsorption configuration of NO<sub>2</sub> on Pb-HTT viewed along the (c) *b*-axis and (d) *c*-axis; electron density difference of the corresponding model viewed along the (e) *b*-axis and (f) *c*-axis. Pink indicates electron accumulation and yellow indicates electron depletion. The isovalue was set to be 0.0003 e Å<sup>-3</sup>.

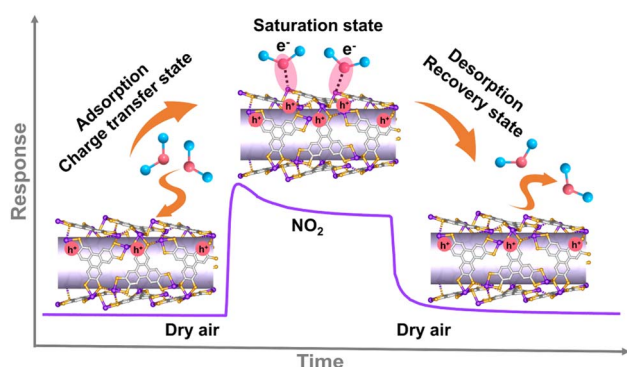


Fig. 5 Proposed sensing mechanism of Pb-HTT toward NO<sub>2</sub>.

## Conclusions

In conclusion, metal-nonmetal-based secondary interactions were proposed for the first time to be a useful tool in structure construction and demonstrated by the construction of a single-crystal nanotubular array **Pb-HTT**. Considerable Pb⋯S secondary interactions helped construct a 1D channel and block the coordination among neighboring nanotubes simultaneously for the construction of **Pb-HTT** MO-CNA. Meanwhile, Pb⋯S secondary interactions also endowed **Pb-HTT** with high thermal/chemical stability and guest-accessible open metal sites. Besides these, **Pb-HTT** also showed a typical semi-conductive nature. As an exemplary application, **Pb-HTT** exhibited the best sensing performances with both a response time <0.1 min and theoretical LOD <0.1 ppb in comparison to all reported room-temperature NO<sub>2</sub> sensing materials. The experimental XANES spectra and theoretical calculations

revealed the exact sensing active sites on **Pb-HTT** and the sensing mechanism. The strategy employed in this work to assemble MO-CNAs and the extraordinary chemiresistive gas sensing performance of **Pb-HTT** undoubtedly shed light on the rational design of functional MO-CNAs.

## Author contributions

Jieying Hu and Jian-Ze Xiao contributed equally to this work. Jieying Hu: investigation, data curation, formal analysis; Jian-Ze Xiao: analysis, methodology, validation; Wei-Ming Liao: writing – original draft, funding acquisition; Shoujie Liu: resources; Jianming Li: visualization; Yonghe He: methodology; Lin Yu: resources; Qiaohong Li: software; Gang Xu: supervision, writing – review & editing, funding acquisition; Jun He: writing – review & editing, supervision, funding acquisition, conceptualization.

## Conflicts of interest

The authors declare no conflict of interest.

## Acknowledgements

This work was funded by the National Natural Science Foundation of China (21871061, 22171263, 91961115 and 21901046), the Foundation of Basic and Applied Basic Research of Guangdong Province (2020B1515120024 and 2021A1515010274), Local Innovative and Research Teams Project of Guangdong Pearl River Talents Program (2017BT01Z032), Science and Technology Planning Project of Guangdong Province (2021A0505030066) and Science and Technology Program of Guangzhou (201807010026), the NSF of

Fujian (2021J02017), Fujian Science & Technology Innovation Laboratory for Optoelectronic Information of China (2021ZR101). We also thanked Dr Lai-Hon Chung for editing the paper and Dr Long Jiang from Sun Yat-sen University for SCXRD test.

## References

- 1 M. He, S. Zhang and J. Zhang, *Chem. Rev.*, 2020, **120**, 12592–12684.
- 2 J.-G. Jia and L.-M. Zheng, *Coord. Chem. Rev.*, 2020, **403**, 213083.
- 3 P. Thanasekaran, T.-T. Luo, C.-H. Lee and K.-L. Lu, *J. Mater. Chem.*, 2011, **21**, 13140–13149.
- 4 M. Serra, R. Arenal and R. Tenne, *Nanoscale*, 2019, **11**, 8073–8090.
- 5 D. T. Bong, T. D. Clark, J. R. Granja and M. R. Ghadiri, *Angew. Chem., Int. Ed.*, 2001, **40**, 988–1011.
- 6 J. Tang, X. Wang, J. Zhang, J. Wang, W. Yin, D. S. Li and T. Wu, *Nat. Commun.*, 2021, **12**, 4275.
- 7 X. G. Liu, S. S. Bao, J. Huang, K. Otsubo, J. S. Feng, M. Ren, F. C. Hu, Z. Sun, L. M. Zheng, S. Wei and H. Kitagawa, *Chem. Commun.*, 2015, **51**, 15141–15144.
- 8 T. Shimizu, W. Ding and N. Kameta, *Chem. Rev.*, 2020, **120**, 2347–2407.
- 9 K. Maeda, L. Hong, T. Nishihara, Y. Nakanishi, Y. Miyauchi, R. Kitaura, N. Ousaka, E. Yashima, H. Ito and K. Itami, *J. Am. Chem. Soc.*, 2016, **138**, 11001–11008.
- 10 J. G. Jia, C. C. Zhao, S. S. Bao, L. Q. Wu, G. H. Wen, A. J. Jacobson, J. Ma and L. M. Zheng, *J. Am. Chem. Soc.*, 2021, **143**, 17587–17598.
- 11 K.-I. Otake, K. Otsubo, T. Komatsu, S. Dekura, J. M. Taylor, R. Ikeda, K. Sugimoto, A. Fujiwara, C.-P. Chou, A. W. Sakti, Y. Nishimura, H. Nakai and H. Kitagawa, *Nat. Commun.*, 2020, **11**, 843.
- 12 J. Tian, L. Liu, K. Zhou, Z. Hong, Q. Chen, F. Jiang, D. Yuan, Q. Sun and M. Hong, *Chem. Sci.*, 2020, **11**, 9818–9826.
- 13 C. R. Murdock and D. M. Jenkins, *J. Am. Chem. Soc.*, 2014, **136**, 10983–10988.
- 14 D. K. Unruh, K. Gojdas, A. Libo and T. Z. Forbes, *J. Am. Chem. Soc.*, 2013, **135**, 7398–7401.
- 15 W. Liu, R. Yin, X. Xu, L. Zhang, W. Shi and X. Cao, *Adv. Sci.*, 2019, **6**, 1802373.
- 16 S. Shin, S. Lim, Y. Kim, T. Kim, T. L. Choi and M. Lee, *J. Am. Chem. Soc.*, 2013, **135**, 2156–2159.
- 17 G. Q. Kong, S. Ou, C. Zou and C. D. Wu, *J. Am. Chem. Soc.*, 2012, **134**, 19851–19857.
- 18 Y.-W. Zhao and X.-M. Zhang, *J. Mater. Chem. C*, 2020, **8**, 4453–4460.
- 19 I. Roy and J. F. Stoddart, *Acc. Chem. Res.*, 2021, **54**, 1440–1453.
- 20 S. K. Sahu, D. K. Unruh, T. Z. Forbes and A. Navrotsky, *Chem. Mater.*, 2014, **26**, 5105–5112.
- 21 G. W. Orr, L. J. Barbour and J. L. Atwood, *Science*, 1999, **285**, 1049–1052.
- 22 Y. Jing, Y. Yoshida, P. Huang and H. Kitagawa, *Angew. Chem., Int. Ed.*, 2022, e202117417.
- 23 Z. Xu, S. Lee, Y.-H. Kiang, A. B. Mallik, N. Tsomaia and K. T. Mueller, *Adv. Mater.*, 2001, **13**, 637–641.
- 24 H. Yuan, J. Tao, N. Li, A. Karmakar, C. Tang, H. Cai, S. J. Pennycook, N. Singh and D. Zhao, *Angew. Chem., Int. Ed.*, 2019, **58**, 14089–14094.
- 25 T. H. Noh and O. S. Jung, *Acc. Chem. Res.*, 2016, **49**, 1835–1843.
- 26 D. Rani, K. K. Bhasin and M. Singh, *ACS Mater. Lett.*, 2019, **2**, 9–14.
- 27 Z. Zhou, C. He, J. Xiu, L. Yang and C. Duan, *J. Am. Chem. Soc.*, 2015, **137**, 15066–15069.
- 28 K. Otsubo, Y. Wakabayashi, J. Ohara, S. Yamamoto, H. Matsuzaki, H. Okamoto, K. Nitta, T. Uruga and H. Kitagawa, *Nat. Mater.*, 2011, **10**, 291–295.
- 29 Y. Zhou, S. Yao, Y. Ma, G. Li, Q. Huo and Y. Liu, *Chem. Commun.*, 2018, **54**, 3006–3009.
- 30 J. M. Ryan and Z. Xu, *Inorg. Chem.*, 2004, **43**, 4106–4108.
- 31 F. Caruso, M. L. Chan and M. Rossi, *Inorg. Chem.*, 1997, **36**, 3609–3615.
- 32 S. C. Pal, D. Mukherjee, R. Sahoo, S. Mondal and M. C. Das, *ACS Energy Lett.*, 2021, **6**, 4431–4453.
- 33 B. Wang, R.-B. Lin, Z. Zhang, S. Xiang and B. Chen, *J. Am. Chem. Soc.*, 2020, **142**, 14399–14416.
- 34 Q. Lin, Y. Ye, L. Liu, Z. Yao, Z. Li, L. Wang, C. Liu, Z. Zhang and S. Xiang, *Nano Res.*, 2020, **14**, 387–391.
- 35 U. M. Shrestha, K. M. Vailonis, D. M. Jenkins and M. D. Dadmun, *ACS Appl. Nano Mater.*, 2020, **3**, 5605–5611.
- 36 J. Zheng, Z. Lu, K. Wu, G. H. Ning and D. Li, *Chem. Rev.*, 2020, **120**, 9675–9742.
- 37 Y. He, J. Huang, J. He and Z. Xu, *J. Visualized Exp.*, 2018, e57455.
- 38 J. H. Huang, Y. H. He, M. S. Yao, J. He, G. Xu, M. Zeller and Z. T. Xu, *J. Mater. Chem. A*, 2017, **5**, 16139–16143.
- 39 D. L. Turner, T. P. Vaid, P. W. Stephens, K. H. Stone, A. G. Dipasquale and A. L. Rheingold, *J. Am. Chem. Soc.*, 2008, **130**, 14–15.
- 40 A. Bondi, *J. Phys. Chem.*, 2002, **68**, 441–451.
- 41 R. B. Lin, Y. He, P. Li, H. Wang, W. Zhou and B. Chen, *Chem. Soc. Rev.*, 2019, **48**, 1362–1389.
- 42 M. Ding, X. Cai and H. L. Jiang, *Chem. Sci.*, 2019, **10**, 10209–10230.
- 43 A. L. Spek, *Acta Crystallogr., Sect. D: Biol. Crystallogr.*, 2009, **65**, 148–155.
- 44 Q. Q. Ge, J. Y. Shao, J. Ding, L. Y. Deng, W. K. Zhou, Y. X. Chen, J. Y. Ma, L. J. Wan, J. Yao, J. S. Hu and Y. W. Zhong, *Angew. Chem., Int. Ed.*, 2018, **57**, 10959–10965.
- 45 J. Tauc, R. Grigorovici and A. Vancu, *Phys. Status Solidi*, 1966, **15**, 627–637.
- 46 E. A. Davis and N. F. Mott, *Philos. Mag.*, 1970, **22**, 903–922.
- 47 D. Liang, L. Shi, J. Zhao, P. Liu, J. A. Sarnat, S. Gao, J. Schwartz, Y. Liu, S. T. Ebel, N. Scovronick and H. H. Chang, *Innovation*, 2020, **1**, 100047.
- 48 C. Copat, A. Cristaldi, M. Fiore, A. Grasso, P. Zuccarello, S. S. Signorelli, G. O. Conti and M. Ferrante, *Environ. Res.*, 2020, **191**, 110129.
- 49 H. Xu, J. Zhang, A. U. Rehman, L. Gong, K. Kan, L. Li and K. Shi, *Appl. Surf. Sci.*, 2017, **412**, 230–237.

- 50 S. Li, M. Wang, C. Li, J. Liu, M. Xu, J. Liu and J. Zhang, *Sci. China Mater.*, 2018, **61**, 1085–1094.
- 51 P. Li, H. Zhan, S. Tian, J. Wang, X. Wang, Z. Zhu, J. Dai, Y. Dai, Z. Wang, C. Zhang, X. Huang and W. Huang, *ACS Appl. Mater. Interfaces*, 2019, **11**, 13624–13631.
- 52 J. Tan, J. Hu, J. Ren, J. Peng, C. Liu, Y. Song and Y. Zhang, *Chin. Chem. Lett.*, 2020, **31**, 2103–2108.
- 53 H. Liu, M. Li, O. Voznyy, L. Hu, Q. Fu, D. Zhou, Z. Xia, E. H. Sargent and J. Tang, *Adv. Mater.*, 2014, **26**, 2718–2724.
- 54 R. Wu, J. Hao, S. Zheng, Q. Sun, T. Wang, D. Zhang, H. Zhang, Y. Wang and X. Zhou, *Appl. Surf. Sci.*, 2022, **571**, 151162.
- 55 H. Bai, H. Guo, J. Wang, Y. Dong, B. Liu, Z. Xie, F. Guo, D. Chen, R. Zhang and Y. Zheng, *Sens. Actuators, B*, 2021, **337**, 129783.
- 56 H. Kan, M. Li, J. Luo, B. Zhang, J. Liu, Z. Hu, G. Zhang, S. Jiang and H. Liu, *IEEE Sens. J.*, 2019, **19**, 846–851.
- 57 Z. Wang, T. Zhang, T. Han, T. Fei, S. Liu and G. Lu, *Sens. Actuators, B*, 2018, **266**, 812–822.
- 58 L. He, W. Zhang, H. Wu and Y. Zhao, *ACS Appl. Nano Mater.*, 2021, **4**, 3998–4006.
- 59 L. He, H. Lv, L. Ma, W. Li, J. Si, M. Ikram, M. Ullah, H. Wu, R. Wang and K. Shi, *Carbon*, 2020, **157**, 22–32.
- 60 Y. Wen, G. E. Wang, X. Jiang, X. Ye, W. Li and G. Xu, *Angew. Chem., Int. Ed.*, 2021, **60**, 19710–19714.
- 61 A. Bag, M. Kumar, D.-B. Moon, A. Hanif, M. J. Sultan, D. H. Yoon and N.-E. Lee, *Sens. Actuators, B*, 2021, **346**, 130463.
- 62 S. Jensen, K. Tan, L. Feng, J. Li, H. C. Zhou and T. Thonhauser, *J. Am. Chem. Soc.*, 2020, **142**, 16562–16568.
- 63 J. Oktawiec, H. Z. H. Jiang, A. B. Turkiewicz and J. R. Long, *Chem. Sci.*, 2021, **12**, 14590–14598.
- 64 S. Bordiga, F. Bonino, K. P. Lillerud and C. Lamberti, *Chem. Soc. Rev.*, 2010, **39**, 4885–4927.
- 65 Y. M. Jo, K. Lim, J. W. Yoon, Y. K. Jo, Y. K. Moon, H. W. Jang and J. H. Lee, *ACS Cent. Sci.*, 2021, **7**, 1176–1182.